Applied Materials Today 21 (2020) 100801

Contents lists available at ScienceDirect

Applied Materials Today

journal homepage: www.elsevier.com/locate/apmt

Three-phase hybrid facilitated transport hollow fiber membranes for enhanced CO_2 separation

Saravanan Janakiram[a], Juan Luis Martín Espejo[a], Karen Karolina Høisæter[a], Arne Lindbråthen[a], Luca Ansaloni[b], Liyuan Deng[a,*]

[a] Department of Chemical Engineering, Norwegian University of Science and Technology (NTNU), Trondheim, NO-7491, Norway
[b] Department of Sustainable Energy Technology, SINTEF Industry, 0373 Oslo, Norway

ARTICLE INFO

Article history:
Received 2 July 2020
Revised 13 August 2020
Accepted 17 August 2020

Keywords:
Facilitated transport
CO_2 separation
Hollow fiber membrane
Graphene oxide
Mobile carriers

ABSTRACT

The configuration of thin film composite (TFC) in the form of hollow fiber is desired for gas separation membranes to achieve better gas permeation and higher packing density. In this work, we developed and tested TFC hollow fiber membranes with a defect-free, ultrathin (200 nm) hybrid facilitated transport selective layer consisting of three phases, i.e., a host polymeric matrix with fixed-site carriers, a 2D inorganic filler, and, a CO_2-philic mobile carrier. The effect of lateral size of graphene oxide (GO)-based fillers on CO_2 permeation were studied in detail, and the modified size-optimized porous GO (pGO) fillers were found to enhance CO_2 permeation at a very low loading of 0.2 wt%. The optimized hybrid materials were then combined with selected mobile carriers, which interact with CO_2 reversibly to form carbonate/carbene-CO_2 adduct to further enhance the CO_2 permeation performance. The resulting hybrid facilitated transport membranes with mobile carriers showcase a CO_2 permeance of up to 825 GPU with a CO_2/N_2 separation factor of 31 and a CO_2/CH_4 of 20. These membranes also exhibit increased resistance to carrier saturation phenomena typical of facilitated transport membranes, showing potential for CO_2 separation applications also at elevated pressures.

1. Introduction

Membranes offer a potential solution for applications related to CO_2 separation due to their high modularity, lower footprint, easier up-scaling, and lower environmental impact when compared to conventional amine-based absorption systems [1–4]. In order to be competitive and industrially attractive for gas separation applications, membranes should be characterized with high permeability and selectivity. Traditional polymeric membrane materials suffer from an inherent permeability-selectivity "trade-off", which limits the separation performance, reducing the commercialization potential of membrane technology despite the low-cost and easy scalability benefits [5,6].

Research efforts on developing high performance membrane materials to overcome the trade-off are mainly focused on increasing permeability and selectivity through various approaches [7–11], such as engineering hybrid materials to combine the advantages of inorganic nanofillers and incorporating CO_2 reactive carriers in polymer matrices for facilitated transport of CO_2. Nonetheless, these developed materials have usually been reported as self-standing thick films, typically in the order of microns. However, the successful development of membrane materials is benchmarked with improvements in transmembrane CO_2 flux (permeance), which reduces the effective membrane area required to achieve targeted separation [12–14]. Such membranes are, in general, fabricated in the form of thin film composite (TFC) as flat-sheet or hollow fiber membranes with a stable, selective layer typically with a thickness of a few hundred nanometers [15].

Typical challenges accompanying the fabrication of ultrathin membranes include retention of the permeation properties of the material that is previously developed and evaluated as self-standing thick films. Additionally, when the selective layer is composed of a hybrid material, the presence of two distinct phases increases the complexity of achieving defect-free coating, while in hollow fiber configuration, the coating procedure needs further optimization due to their curved topology [16].

Limited studies have been reported on fabricating hollow fiber thin composite membranes with a hybrid selective layer for CO_2 separation applications. Dai et al. [17] have embedded ZIF-8 nanofillers of 200 nm size in Ultem® 1000 (polyetherimide) polymer, resulting in an asymmetric hollow fiber membrane with a

* Corresponding author
E-mail address: liyuan.deng@ntnu.no (L. Deng).

https://doi.org/10.1016/j.apmt.2020.100801

CO_2 permeance of 30 GPU with CO_2/N_2 separation factor of 25 under mixed gas conditions. Smaller sized ZIFs (less than 100 nm) were dispersed in Pebax polymer by Sutrisana et al. [18] in the form of hollow fibers to increase the plasticization resistance obtaining stable CO_2 permeance of 350 GPU with the corresponding CO_2/N_2 selectivity of 32. Zhang et al. [19] reported a CO_2 permeance of 415 GPU with CO_2/N_2 separation factor of 43 using graphene oxide (GO) in Pebax coated on PVDF hollow fibers albeit with characterization only by single gas tests.

There exist a variety of nanofillers that enhance CO_2 permeation properties in conventional polymeric membranes. Both 1D nanofillers like nanocellulose [20,21] and 2D materials like GO [22] have been successfully used in polymeric matrices in the form of hybrid membranes for CO_2 separation, exploiting their high aspect ratio geometries [1,8]. Nevertheless, polymeric membranes containing such fillers are seldom studied as hybrid membranes in the form of thin composite hollow fibers with ultra-thin selective layers. Hollow fiber membranes are particularly interesting for gas separation due to their maximum achievable packing density. The high surface-to-volume ratio arising from the 2D structure triggers nanoscopic property changes when dispersed in polymeric matrices. Effective dispersion of these platelets, even under small quantities, affects reorienting of the polymer chain packing, inducing changes in crystallinity, fractional free volume and CO_2 solubility [23]. The use of a very small loading of these 2D fillers helps in coating defect-free hybrid selective layers for TFC membranes, but their high aspect ratio can still pose a considerable challenge for hollow fiber configuration.

Another approach to overcome the permeability-selectivity "trade-off" is by introducing CO_2-reactive carriers into the polymeric selective layer. The so-called "facilitated transport" membranes transfer CO_2 through an additional reactive pathway compared with conventional polymers that follow the solution-diffusion mechanism only [24]. The reactive carriers are typically amine groups fixed to the backbone of the polymeric chain. Facilitated transport is found beneficial in low-pressure applications like post-combustion capture [9], as the reactive sites become saturated at higher CO_2 partial pressures in the feed [25]. This phenomenon, known as "carrier saturation", leads to an eventual reduction in permeation performance of facilitated transport membranes for applications that involve elevated feed pressures. Small CO_2-philic molecules that reversibly react with CO_2 can be added to the polymeric host matrices as "mobile carriers" to increase CO_2 transport [26]. The low molecular weight of these compounds leads to an increase in the density of CO_2-reactive groups in the membrane matrix and can help in combating the carrier saturation phenomena. Nonetheless, the reactions with carriers require water to aid CO_2 transport across the membrane. Conveniently, GO nanosheets being hydrophilic, induce the polymer chain disruption when added to facilitated transport matrices, leading to distributed water-rich channels and increased CO_2 solubility. These synergistic effects of GO and mobile carriers on the gas separation properties of such hybrid membranes rely highly on the distribution and surface chemistry of the added nanosheets as well as their lateral dimensions in addition to the properties of the mobile carrier.

In this work, we report the first three-phase hybrid facilitated transport membranes (HFTMs) in TFC hollow fiber configuration with outstanding separation performance. Sterically hindered polyallylamine (SHPAA) was used as the facilitated transport polymer matrix and GO-based 2D nanoplatelets were embedded as nanofillers, which were both size-optimized and physically modified to favour gas transport properties upon dispersion in the membrane matrix. Water-soluble mobile carrier phases comprising of CO_2-reactive small molecules were optimized and studied for their interaction with CO_2. The optimal content of the mobile carriers in the polymeric matrix to benefit CO_2 transport were determined. Ultrathin selective layers less than 200 nm were coated as hollow fiber membranes. The fabricated membranes were tested for CO_2/N_2 separation at 1.7 bar and CO_2/CH_4 separation at elevated pressures (up to 20 bar) to simulate flue gas and biogas conditions, respectively. The effect of feed pressure on CO_2/CH_4 separation properties was also studied.

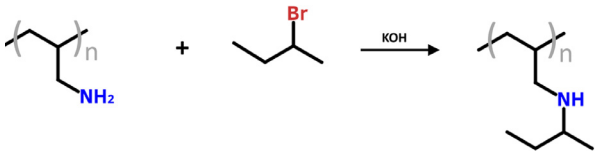

Scheme 1. Steric hindrance of polyallylamine.

2. Materials and methods

2.1. Materials

Poly(allylamine hydrochloride) (Mw = 120,000–200,000) was bought from Thermo Fisher Scientific, Sweden. 2-bromobutane (≥98%, Mw = 137.02) purchased from Sigma-Aldrich, Norway was used for the synthesis of SHPAA. Graphene Oxide dispersion (2.5 wt% in water) was supplied by Graphene-XT, Italy and used as diluted dispersions. Hydrogen peroxide (H_2O_2, 30% in water) used in the synthesis of porous Graphene Oxide (pGO) was supplied by Sigma-Aldrich, Norway. L-proline Reagentplus® (≥99 wt%), 1-(2-Aminoethyl) piperazine (99 wt%), 1-Ethyl-3-methylimidazolium acetate (97 wt%) and sarcosine (N-Methylglycine) (98 wt%) were purchased from Sigma-Aldrich, Norway. Potassium hydroxide (pellets, 99.9%), polyvinyl alcohol (Mw = 89,000–98,000, 89% hydrolyzed), Deuterium oxide (99.9%), 3-(Trimethylsilyl) propionic-2,2,3,3-d_4 acid sodium salt (TMSP, 98%) were used as received from Sigma-Aldrich, Norway. Poly(p-phenylene oxide) (PPO) hollow fibers used as coating supports (inside diameter of 350 µm and outside diameter of 540 µm) were obtained from Parker A/S Norway. CO_2/N_2 mixture (10 vol.% CO_2 in N_2), CO_2/CH_4 mixture (40 vol.% CO_2 in CH_4), and CH_4 (99.95%), that were used for permeation tests were supplied by AGA, Norway.

2.2. Methods

2.2.1. Synthesis of sterically hindered polyallylamine

Polyallylamine hydrochloride was purified by reacting with equivalent amounts of KOH in MeOH, precipitating KCl in a one-step process. Subsequently, purified PAA was modified into poly-N-isobutyl allyl amine (SHPAA) by reaction with an equivalent amount of 2-bromobutane and KOH in MeOH at 50 °C (Scheme 1). The resulting polymer was purified by separating precipitated KCl crystals followed by drying in a N_2 atmosphere at 60 °C.

2.2.2. Synthesis of nanofillers

The GO dispersion as received was first diluted to 1 mg g^{-1} solution followed by pH adjustment to 10 using 1M NaOH. The diluted solution was sonicated in a bath sonicator for 30 min at 25 °C. The dispersion is then subject to ultrasonic disintegration (Vibra-Cell™ Ultrasonic Liquid Processor) at an amplitude of 60% in an ice bath with a 3-s pulse followed by a 2-s break. This procedure was carried out to simultaneously exfoliate and control the size of GO flakes by varying the time of operation. In this study, the sonication was carried out for 3, 6 or 9 h, and the resulting GO flakes were referred to as GO3, GO6, and GO9, respectively. Furthermore, these size-controlled GO dispersions were then hydrothermally treated to introduce random non-selective pores as described by Lee et al. and Xu et al. [27,28]. The GO dispersion was

mixed with 3 wt% H_2O_2 solution, and the mixture was stirred vigorously for 10 min followed by bath sonication for 10 min. Thereupon, the mixture is treated in a Teflon autoclave for 6 h at 180 °C. The resulting pGO dispersions derived from GO3, GO6 and GO9 samples were named as pGO3, pGO6 and pGO9, respectively.

2.2.3. Synthesis of mobile carriers

Mobile carriers considered in this work are two amino acid salts and an ionic liquid. Equivalent amounts of ι-proline and KOH were dissolved in DI water to form a solution of 10 wt% total solids. The solution was then stirred at high speed (~800 rpm) at room temperature for 12 h to form potassium L-prolinate (ProK).

Similarly, equivalent amounts of 1-(2-Aminoethyl) piperazine and sarcosine were stirred in calculated quantities of DI water at room temperature to obtain 37.7 wt% of 2-(1-piperazinyl) ethylamine sarcosinate (PZEA-SARC).

1-Ethyl-3-methylimidazolium acetate ([Emim][OAc]) was dissolved in DI water to form a 10 wt% solution and stirred overnight at room temperature.

2.2.4. Coating of hollow fiber membranes

Purified and dried SHPAA after modification was dissolved in DI water to obtain a 6 wt% solution, and the polymer solution was stirred for at least 2 days at room temperature to obtain a clear polymer solution. In the case of PVA, a 4 wt% solution was prepared by dissolving PVA pellets in DI water at 80 °C for 4 h under reflux conditions. A polymer blend of SHPAA and PVA in the weight ratio of 9:1 was used in all the membranes. PVA was added due to its excellent film-forming abilities.

For casting solution preparation, calculated quantities of polymer solutions were added to DI water and diluted to a casting solution concentration of 0.15 wt% polymer. The amounts of mobile carriers were reported as the composition of mobile carriers in the total organic content (polymer + mobile carrier), while the amounts of nanofillers, which are considered as additives to the organic matrix, were reported as their loadings in terms of total organic solid content (including the polymer and mobile carriers), as described in Eqs. (1) and (2), respectively.

$$c_{mc} = 100 \times \left[\frac{w_{mc}}{w_{pol} + w_{mc}} \right] \quad (1)$$

$$c_{nf} = 100 \times \left[\frac{w_{nf}}{w_{pol} + w_{mc}} \right] \quad (2)$$

where w_{mc} is the weight of mobile carrier (g), w_{pol} is the total weight of the dry polymer (g), and w_{nf} is the weight of nanofiller (g). c_{mc} is the composition of mobile carriers to the organic phase (wt%), and c_{nf} is the loading of the nanofiller (wt%).

For facilitated transport membranes with mobile carriers, calculated quantities of the mobile carrier solutions were first diluted with water followed by drop-wise addition of polymer solutions, so that the overall solid content (polymer + mobile carrier) remained at 0.15 wt%. For HFTMs, both GO and pGO nanofillers were dispersed in SHPAA/PVA solution at two filler loadings of 0.2 wt% and 0.5 wt%. For HFTMs with mobile carriers, lean dispersions of nanofillers were initially prepared, followed by drop-wise addition of both mobile carrier solutions and subsequently polymer solutions in calculated quantitates.

PPO hollow fiber membranes were used as substrates to fabricate hollow fiber membranes. The chosen PPO supports have a thin unselective skin layer that helps in coating the ultrathin selective layer with low molecular weight additives. The skin layer also prevents pore penetration and acts as additional mechanical support to the selective layer, especially at high pressure feed conditions. The PPO supports were hung vertically with the ends sealed using paper clips, which also creates tension and avoids slackening of fibers. DI water was used to wash the fibers twice to remove possible dust particles sticking to the surface, followed by drying in air at room temperature. The thin selective layer was achieved by dip coating the fibers using the casting solution in both directions at a constant low speed (in the range of 6–8 cm s^{-1}) with a time interval of 30 min between successive coating procedures. Coating in opposite directions ensures defect-free selective layer. Additionally, the lean viscosity of casting solution owing to the low solid content leads to uniformity of selective layer thickness independent of coating speed and filler loading. The fibers were then dried at room temperature first, followed by drying at 60 °C under vacuum for 2 h to remove residual solvent components. The resulting fibers exhibit a shiny appearance due to the presence of ultrathin selective layer coating.

In order to assemble the coated hollow fiber (HF) membranes into a module, a few fibers (in the range of 2–5) were inserted carefully into a pre-assembled stainless-steel HF module designed using ¼ inch ⅜ -inch Swagelok™ fittings. The ends were then sealed using epoxy adhesive. The bore side of the fibers was opened by breaking off the cured adhesive on an extension mould.

2.3. Material and membrane characterization

2.3.1. Nanofiller characterization

Fourier-transform infrared (FTIR) spectroscopy was used to determine changes in the chemical structure of the GO nanofillers during the ultrasound treatment. This was done by using a Thermo Nicolet Nexus spectrometer equipped with a smart endurance reflection cell with a diamond crystal in attenuated total reflectance mode. The spectra were built averaging 16 scans with a resolution of 4 cm^{-1} between the range of 4000 cm^{-1} and 800 cm^{-1}. The same procedure was used to study the interaction of CO_2 with PZEA-Sarc, as the loaded solution formed solid precipitates. A 30 wt% solution of PZEA-Sarc was used for the studies. For obtaining spectra of nanofillers, 5– 10 mL of 1 mg g^{-1} dispersions of the nanofillers were dried on a microscope glass slide in the ventilated oven at 60 °C. A clean slide was used for obtaining the background spectra, followed by analysis with the slides containing deposited nanofillers.

Renishaw InVia Reflex Spectrometer system was used for obtaining Raman Spectra of GO nanofillers using 532 nm wavelength incident laser in the range of 3200 cm^{-1} and 100 cm^{-1}. Laser intensity was varied between 5–20% based on the response by the samples to signal. The samples were prepared by drying a few drops of GO/pGO dispersions on a microscopic slide followed by drying in the ventilated oven at 60 °C.

The GO and pGO nanosheets were imaged using a Scanning Transmission Electron Microscope (S(T)EM, Hitachi S-5500, Hitachi High Technologies America, Inc., USA). The bright field detector was used for transmission measurements. The samples were prepared by dispersing a drop of dilute dispersions on 300 mesh Cu grids (Electron Microscopy Sciences, FCF300-Cu).

Topographic analysis of nanofillers was done using an Atomic Force Microscope (AFM) (AFM Dimension Icon, Bruker, USA). The samples were prepared by drying a drop of dispersion on freshly cleaved Mica sheets followed by drying at room temperature. The imaging was done in Scan Asyst QNM tapping mode using a silicon nitride tip.

2.3.2. Characterization of mobile carriers

For the thermal stability evaluation of mobile carriers loaded in the polymer matrices, films with various mobile carrier content were made and tested in a thermogravimetric analyser (TGA, TG 209 F1 Libra, Netzsch, Germany). About 10–15 mg of the samples were loaded in a ceramic crucible and heated at a constant rate of 20 K min^{-1} under N_2 atmosphere (purge rate 60 ml min^{-1}) from

room temperature to 800 °C. The corresponding changes in mass were recorded as a function of temperature.

To identify the interactions of CO_2 with mobile carriers, liquid-state NMR was used. The NMR experiments were performed on a Bruker 600 MHz Avance III HD spectrometer equipped with a 5 mm cryogenic CP-TCI z-gradient probe. The obtained spectra were analysed in the software Bruker TopSpin 4.0.7. The samples for NMR were prepared by bubbling CO_2 at room temperature in mobile carrier solutions (65% [Emim][OAc] in D_2O/H_2O; 10% ProK in H_2O) for a period of 24 h–48 h. Deuterated water was used as the "lock" solvent, and TMSP was used as an internal reference standard. The loaded ProK solution was placed in an NMR tube, and the lock solvent was placed in an inserted coaxial insert. To be able to lock [Emim][OAc] containing samples, this configuration was reversed. The loaded solution was placed in a coaxial insert, which was then placed inside an NMR tube filled with the "lock" solvent.

2.3.3. Membrane characterization

Field Emission SEM APREO (FEI, Thermo Fisher Scientific, USA) equipped with an in-lens detector under both standard and immersion mode was used for structural and morphological analysis of the membranes. Samples for cross-sectional analysis of HF were obtained by freeze-fracturing in liquid N_2. All samples were coated with a few nanometers of Pd/Pt alloy prior to measurements to increase the sample conductivity.

2.3.4. Gas permeation performance

The fabricated HF membranes were evaluated for gas permeation performance using humid mixed gas permeation test rigs, as reported in our previous studies [20,21]. The feed composed of 90/10 v/v CO_2/N_2 mixture or 40/60 v/v CO_2/CH_4 mixture. The flow rate of the feed was 300 ml min^{-1} for the CO_2/N_2 tests and 400–600 ml min^{-1} for the CO_2/CH_4 tests. The difference in feed flow rates was mainly to recoup differences in membrane areas and targeting a very low stage cut of below 5%. The sweep gas for CO_2/N_2 tests was CH_4, while for the CO_2/CH_4 tests, N_2 was used as the sweep gas. In both cases, feed and the sweep gas streams were humidified in a bubble tank before the membrane module. The shell side of the membranes was used for the feed gas and the bore side of the fibers was used as the permeate/sweep side. The pressure on the feed side was maintained constant at 1.7 bar for the CO_2/N_2 tests and varied between 2 to 20 bar for the CO_2/CH_4 tests. Sweep side pressure was held at 1.02 bar. The temperature of operation was maintained at 35 °C for all tests. The exit gas compositions in both feed and sweep side were monitored continuously using a calibrated gas chromatograph (490 Micro GC, Agilent, for CO_2/N_2 tests and MG5, SRI Instruments Inc., for CO_2/CH_4 tests). The permeance of component '*i*' was obtained using the following equation

$$P_i = \frac{V_p(1 - y_{H_2O})y_i}{\left(< p_{i,f}, p_{i,r} > - p_{i,p}\right)A} \quad (3)$$

where the total permeate flow V_p is in ml s^{-1} measured at the exit using a bubble flow meter at steady-state conditions. y_{H_2O} and y_i denote the molar fraction of the water and permeating species in the permeate flow, respectively. Partial pressures $p_{i,f}$, $p_{i,r}$ and $p_{i,p}$ of the species '*i*' in the feed, retentate, and permeate, respectively, are in cm Hg^{-1}. $p_{i,f}$, $p_{i,r}$ is the average of feed and retentate partial pressure. Permeance of components are represented in GPU, where 1 GPU = 10^{-6} cm^3(STP) cm^{-2} s^{-1} $cmHg^{-1}$ = 3.35 × 10^{-10} mol m^{-2} s^{-1} Pa^{-1}. The separation factor is calculated using concentrations of each component according to the equation

$$\alpha_{i/j} = \frac{y_i/x_i}{y_j/x_j} \quad (4)$$

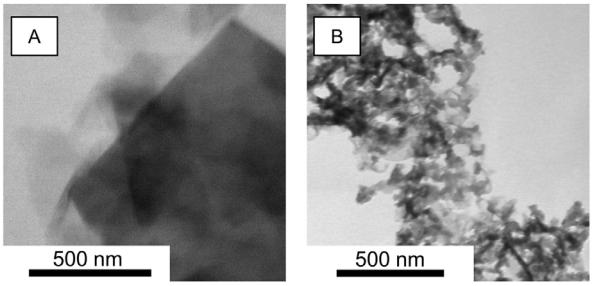

Fig. 1. S(T)EM imaging of (A) GO3 and (B) pGO3.

where *y* and *x* identify the gas content in the permeate and feed side, respectively. The experiments have all been performed at a low stage cut (<5%) to prevent concentration polarization phenomena, which reduces the influence of the module performance and allows retrieval of the material performance.

3. Results and discussion

3.1. Characterization of GO-based nanoplatelets

3.1.1. S(T)EM

The formation of non-selective pores in GO nanosheets through the hydrothermal treatment is confirmed by representative S(T)EM imaging of GO3 and pGO3 as seen in Fig 1. The 2D GO nanosheets seem stacked into a few layers similar to the previous reports in the literature [29,30] The morphology of random non-selective pores shown in Fig. 1B is also confirmed by previous studies [27,28].

3.1.2. AFM

The sonication-assisted exfoliation procedure was employed to obtain monolayers of GO in water dispersion. In order to ensure the reproducibility of the method, the concentration of GO dispersion was kept constant at 2 mg mL^{-1}, and the sample volume was maintained at 300 mL for all procedures. In this study, three sonication durations were chosen to simultaneously reduce the lateral dimensions during the exfoliation process. The sonication process imparts random fragmentation of 2D nanosheets induced by mechanical failure of defective sp^3 regions [31]. These random lacerations are followed by propagation of cracks leading to reduced flake sizes. Several studies have reported the effect of sonication time on the lateral dimensions of GO nanosheets [23,32–34]. Typical studies involve AFM and TEM to analyse the distribution of flake dimensions and aspect ratios. In this study, AFM analysis revealed the presence of large flakes with lateral dimensions of more than 1 µm for GO3. Subsequent sonication resulted in smaller flakes in the range of 400–800 nm and down to less than 500 nm for GO6 and GO9, respectively (Fig. 2A–C). All samples were then subject to hydrothermal treatment to introduce random pores. While size estimation of pGO flakes with AFM was challenging due to their morphology, representative imaging of pGO flakes (pGO6, Fig. 2D) show a further reduction in flake size after the hydrothermal treatment. This size reduction was confirmed with relative increase in presence of carbonyl groups (observed from FTIR) that were exposed along the edges of the pGO when compared to GO.

3.1.3. FTIR

Chemical changes in the GO nanoplatelets during the hydrothermal treatment process was studied using FTIR spectroscopy. The sonication procedures barely affected the chemical structure of the GO and pGO nanoplatelets rendering similar spectra for the

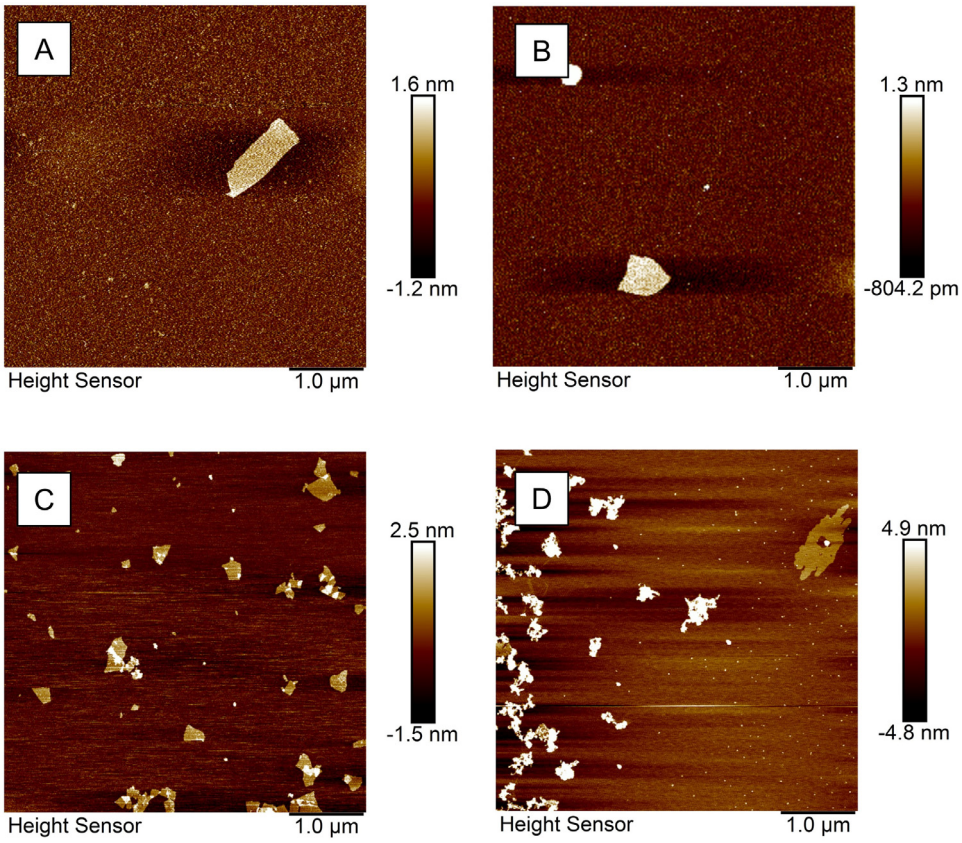

Fig. 2. AFM imaging of representative GO nanosheets used for HF membranes of (A) GO3 (B) GO6 (C) GO9 and (D) pGO6.

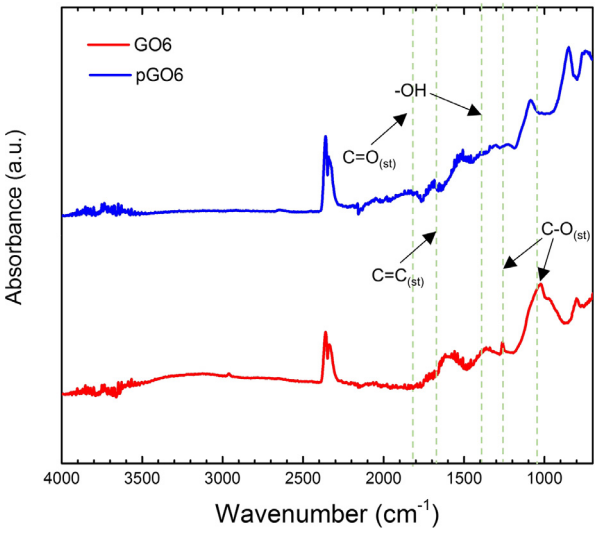

Fig. 3. FTIR spectra of pre-dried GO6 and pGO6.

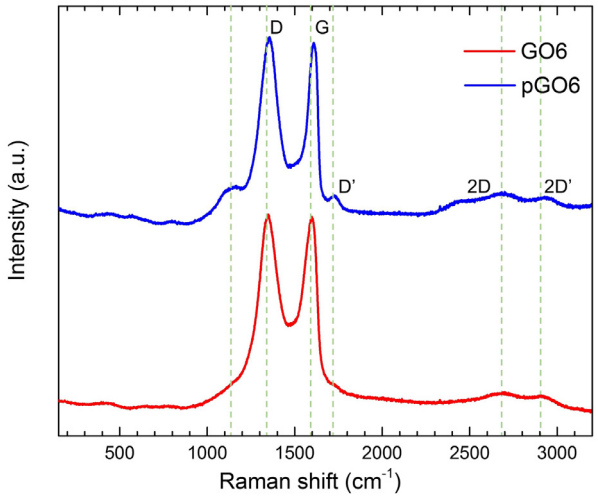

Fig. 4. Raman Spectra at room temperature of GO6 and pGO6 on a glass slide.

family of GO and pGO individually (**Figure S1**). Previous studies report similar results on the chemical composition of 2D materials unaltered with the ultrasonic fragmentation process [32]. However, discernible peak changes appeared between the GO and pGO as seen in Fig. 3. Characteristic GO peaks include -C-O-C- alkoxy stretching at 1050 cm^{-1} and the corresponding epoxy stretching vibration at 1250 cm^{-1}. The peak at 1412 cm^{-1} is assigned to the deformation of surface –OH groups [35]. Since the modification process involves oxidation using hydrogen peroxide, C=O carbonyl stretch was observed at 1723 cm^{-1}, while the other oxygen functional groups were preserved [36]. Interestingly, C=C stretching vibrations were confirmed at 1680 cm^{-1}. These transpolyacetylene segments indicate that the pGO modification procedure also created stabilized end groups at grain boundaries.

3.1.4. Raman spectroscopy

Raman spectra of thin films of GO and pGO deposited on a glass slide were obtained to characterize the structure and quality of various GO and pGO nanofillers. Fig. 4 compares the Raman

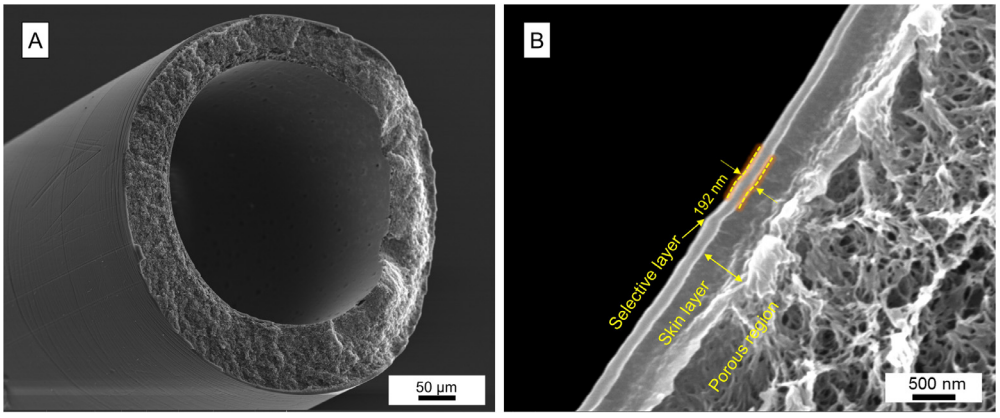

Fig. 5. SEM imaging of neat SHPAA/PVA membrane; the freeze-fractured hollow fiber (A) and cross-section (B).

spectra of representative GO6 and pGO6. The spectrum of GO6 clearly marks 4 active bands: - *D* band at ~1340 cm^{-1} indicating disorder caused by graphite edges; *G* band at ~1570 cm^{-1} indicating in-phase vibration of sp^2 hybridized graphite lattice [37]; two other weak bands (*2D* and *2D'*) associated to *2D*, which is a dispersive overtone of *D* band that also signifies the layering of the GO nanosheets. The splitting of the original *2D* band into overlapping *2D* and *2D'* peaks denote the presence of few-layer graphene planes, confirming successful exfoliation of platelets both in GO and pGO [38].

Two interesting signature peaks around ~1130 cm^{-1} and ~1720 cm^{-1} appeared for all pGO nanofillers. The latter is assigned as *D'* band, which is a result of double resonance Raman process indicative of defective structure [39,40]. The intensity of *D'* band relative to other bands is higher in all pGO samples than GO nanofillers (**Figure S2**), representing increased basal plane defects in line with the expectations. The band at 1130 cm^{-1} has been seldom reported in graphene. It can be assigned to transpolyacetylene species at grain boundaries and surfaces [41] and also associated to the presence of holes created in the GO flakes [42] after the hydrothermal treatment. The presence of transpolyacetylene segments in pGO is also confirmed by the FTIR peak at 1680 cm^{-1} assigned to C=C stretching frequency (Fig. 3). Another important characterization of GO quality in terms of disorderliness attributed to sp^3 in predominantly sp^2 hybridization is studied using the I_D/I_G ratio. The ratio remained similar at ~1 for all GO and pGO samples, denoting no obvious reduction during the sonication or the hydrothermal treatment process (**Figure S2**) [43].

3.2. Morphology of hybrid hollow fiber membranes

Figs. 5 and 6 show the SEM imaging of the cross-section and the outer surface of the hollow fibers coated with the different casting solutions. All mobile carriers formed smooth topologies in the concentrations studied in line with observations made in our previous study[26]. The total solid content in the casting solution was maintained low (0.15 wt%), which resulted in an ultrathin selective layer thickness of ~200 nm on the skin layer of PPO hollow fibers, as seen in Fig. 5B. The facile dip-coating procedure also ensures the in-plane alignment of GO due to shear alignment[19]. The neat polymer membrane and a representative polymer membrane containing 20% Pro-K showcased a rather smooth topography as seen in Figs. 5A and 6A, B. Alternatively, the surfaces of fabricated membranes also exhibited discernible circumferential spots in both GO and pGO containing membranes arising from the boundaries of the underlying platelets (Figs. 6C and 7D).

3.3. Effect of mobile carriers in facilitated transport membranes

In facilitated transport membranes, CO_2 permeates through a reactive pathway in addition to the solution and diffusion mechanism [20,44]. The amine groups attached to the backbone of the polymeric matrix reversibly react with CO_2 in the presence of water to transport CO_2 across the membrane. Although polymers like polyvinylamine and polyallylamine contain a high density of amine groups relative to the hydrocarbon content in the repeating unit of the polymer, their contribution to increased CO_2 transport relies on the access to the amine groups for CO_2 and the proximity to form continuous channels for CO_2 reaction and transfer. In this work, sterically hindered polyallylamine polymer was chosen to increase the accessibility of amine groups to CO_2 [45]. Nevertheless, the amine groups are still locked in the main chain, restricting their mobility in the water-swollen matrix. Hence, to increase the diffusivity of these reactive species, CO_2-philic compounds are added in the matrix as mobile carriers [26]. The addition of these mobile carriers not only increases the density of CO_2-philic moieties in the polymer matrix but also enhances the mobility of CO_2-reacted species, thus increasing CO_2 diffusivity in the host matrix. Important characteristics of such mobile carriers for beneficial use in facilitated transport membranes include (1) low molecular weight (higher mobility), (2) high CO_2 uptake capacity, and (3) capability of formation of weak bond with CO_2 that enhances the transport of CO_2 through water-swollen membrane matrices (reversible CO_2 association/dissociation) and facilitate its release at the permeate side.

Three different CO_2-philic compounds were selected to be used in this study to result in facilitated transport membranes as mobile carriers. The host polymer matrix was loaded with miscible mobile carriers - one ionic liquid ([Emim][OAc]) and two amino acid salts (ProK and PZEA-SARC) with varying amine chemistry. All the mobile carriers are characterized with low vapor pressure and they have sufficient thermal stability as additives for membranes in the considered CO_2 separation applications, as studied using TGA analysis shown in **Figure S3**.

[Emim][OAc], a room-temperature ionic liquid, reacts with CO_2 via carbene route and forms a carbene-CO_2 adduct. The formation of the adduct is confirmed by NMR spectra of the CO_2 bubbled [Emim][OAc] aqueous solution in addition to bicarbonate/carbonate species (**Figure S4**). One of the main advantages of using [Emim][OAc] as mobile carrier compared to the other two amino acids is that its carbene-routed interaction with CO_2 does not influence the viscosity of the solution, which may be beneficial in reducing the mass transfer resistance in the selective layer upon the sorption of CO_2 [46]. The carbene-CO_2 adduct (as shown in

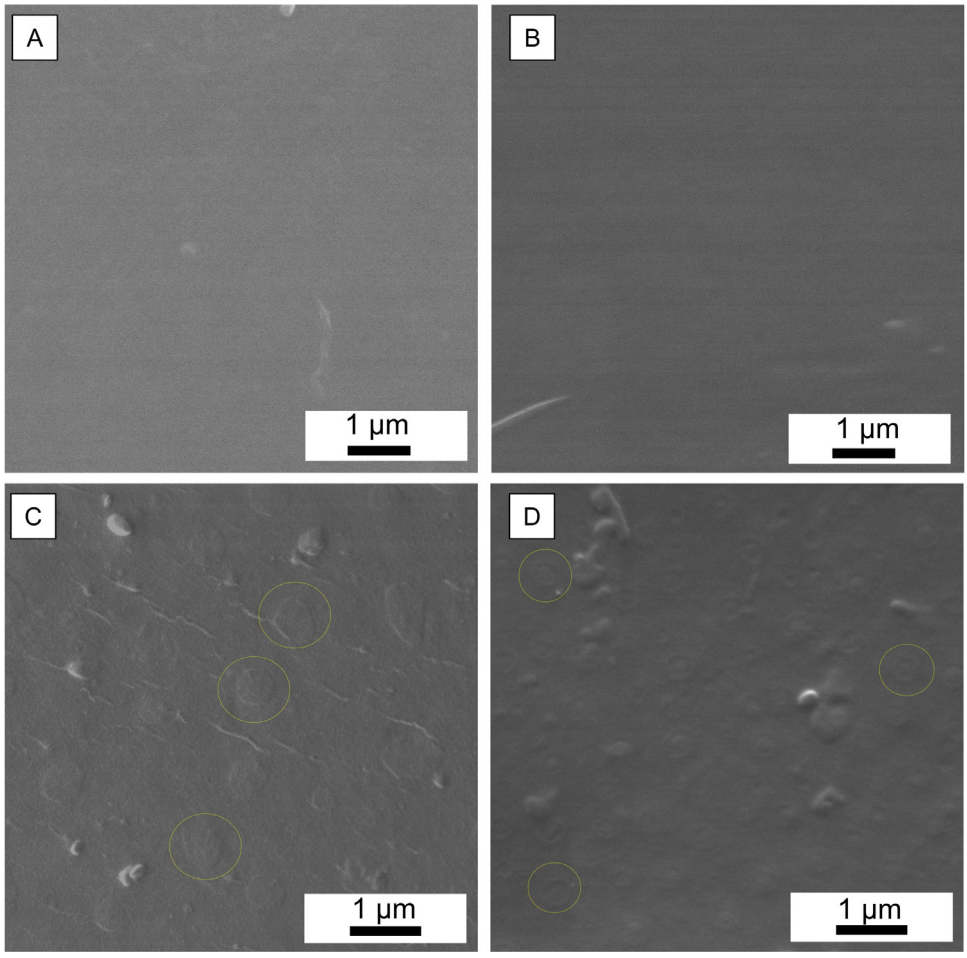

Fig. 6. Surface SEM images of membranes with (A) neat SHPAA/PVA (B) SHPAA/PVA with 20% ProK (C) SHPAA/PVA with 0.2 wt% GO6 (D) SHPAA/PVA with 0.2 wt% pGO6.

Scheme 2A) has also been reported to have faster diffusion despite the bulkiness of the imidazolinium ring due to its planar molecular structure [47]. Additionally, the presence of water inhibits the interaction of the acetate group with CO_2 to form acetic acid, which might result in pH changes in the system [48]. However, above an optimum content of 10 wt%, the ionic liquid was found to reduce the CO_2 transport. This effect can be due to the increased concentration of acetate groups that lead to pH changes upon interaction with CO_2, forming acetic acid, which decreased the efficiency of amine groups present in the host polymer matrix. Nevertheless, at an optimal content of 10 wt%, the CO_2 permeance increased to 716 GPU with a CO_2/N_2 separation factor of 32 (Fig. 7).

ProK (potassium L-prolinate), a secondary amino acid, reacts with CO_2 to form carbamate and bicarbonate/carbonate species [49]. The presence of these species formed upon interaction with CO_2 with the mobile carrier (represented in Scheme 2B) was identified by NMR studies (**Figure S5**). Studies indicate that the formation of carbonate/bicarbonate species is more favoured in ProK than the carbamate intermediate due to the steric hindrance effect [49,50]. Increasing the content of ProK mobile carrier led to increasing CO_2 permeance from 407 GPU to 730 GPU at 20 wt% with no significant change in CO_2/N_2 separation factor, as seen in Fig. 7. Further addition led to marginal changes in CO_2 permeance, which can be attributed to small changes in the thickness of the selective layer with increasing solids in coating solutions [26].

PZEA-Sarc is an amino acid salt containing one primary amine, two secondary amines (one from sarcosine) and one tertiary amine. CO_2 interacts with this mobile carrier to form primary and secondary mono-carbamates (Scheme 2C). Unlike both ProK and [Emim][OAc] where liquid state NMR was used for analysis, PZEA-Sarc crystallized to form semi-solid precipitates upon saturation with CO_2 at 30 wt% concentration in water. Lower reaction time led to undetectable CO_2-loaded compounds in NMR. Hence, FTIR studies were carried out to study the interaction instead of ^1H and ^{13}C NMR with solid precipitates. The presence of carbamate species in aqueous solutions is confirmed by the spectra. (**Figure S6**). The addition of PZEA-SARC increased the CO_2 permeance only at a high content of 30 wt% to 635 GPU when compared to ProK and [Emim][OAc] which can be attributed to more stable and bulky carbamates formed with the interaction of CO_2 and the increased viscosity of CO_2-loaded mobile carriers.

3.4. Effect of nanoplatelets in facilitated transport membranes

Homogeneous dispersions of GO and pGO with varying lateral dimensions enabled successful coating of HFTMs and the resulting membranes were evaluated for CO_2/N_2 separation performances. The resulting gas separation performances of hybrid membranes at two different loadings (0.2 wt% and 0.5 wt%) are summarised in Fig. 8.

Under optimized conditions, both GO and pGO platelets serve in creating fast transport channels for CO_2 due to increased sorption and water channel redistribution due to their large aspect ratio. GO3 is characterized with the highest average lateral dimensions (larger than a micron), and hence the barrier effect contributed to decreased CO_2 permeance at both loadings

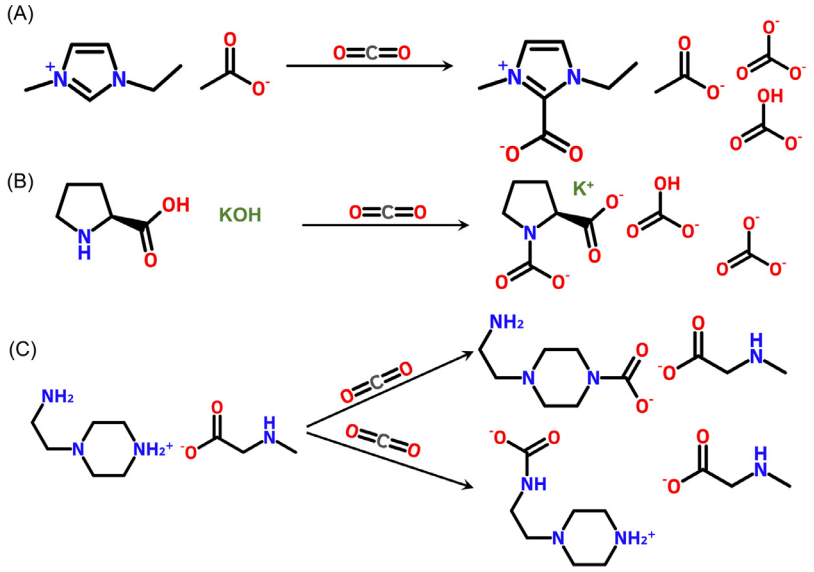

Scheme 2. Interaction of the three mobile carriers with CO_2 (A. [Emim][OAc]; B. ProK; C. PZEA-Sarc).

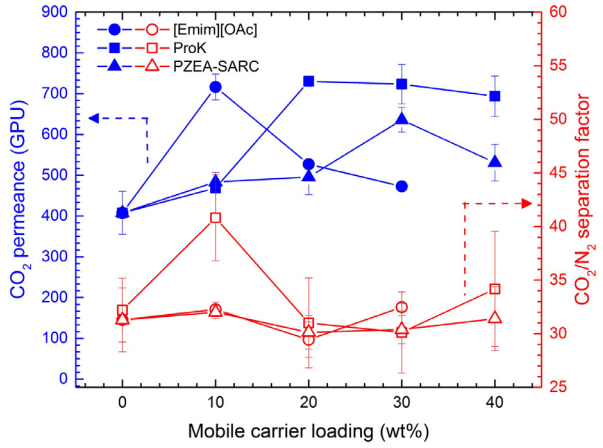

Fig. 7. CO_2/N_2 mixed gas permeation performance of various facilitated transport membranes as a function of mobile carrier content measured at 35 °C, 1.7 bar. (Filled shapes denote CO_2 permeance and empty shapes denote corresponding CO_2/N_2 separation factors).

of nanosheets (Fig. 8A). The corresponding pGO3 at 0.2 wt%, however, increased the CO_2 permeance marginally to 470 GPU due to a drop in the resistance to gas transport due to in-plane pores (Fig. 8B). The further addition of fillers leads to a drop in CO_2 permeance, which can be attributed to the increased barrier effect of GO due to the larger nanosheet size. GO6 and pGO6 hybrids exhibited a sharp increase in CO_2 permeance at 0.2 wt% to 530 GPU and 780 GPU, respectively (Fig. 8A and B). This phenomenon can be attributed to the optimal lateral dimensions of the GO platelets studied. Pristine GO nanosheets are renowned for their barrier efficacy as their high aspect ratio inflict resistance to gas transport. Hence in hybrid matrices, the average platelet size plays a pivotal role. For instance, large-size GO effectively imparts changes in polymer- or polymer-GO interface in favour of gas transport, but also simultaneously increases barrier effect for gas transport by increasing the diffusion pathways. On the other hand, a similar effect can be expected in the corresponding pGO nanofiller, which, however, offers reduced resistance to CO_2 transport through the non-selective pores while the preserved 2D structure still imparts property changes in polymer chains in the surrounding environment. Additionally, the increased exposure of edge groups can also contribute to higher CO_2 affinity. The amount of these edge groups is inversely proportional to the average lateral dimensions [51]. Consequently, the appropriate average lateral dimensions of GO6 and pGO6 present the optimal effect, leading to higher CO_2 permeance when compared to the other fillers at the same loading.

Thus, the composition of 0.2 wt% nanofiller marked optimal nanosheet dimensions and loading where the exposition of edge groups and disruption of chain packing (which is dependent on flake size and dispersion) reach the maximum, simultaneously overcoming the barrier resistance to gas permeation induced by the GO/pGO basal planes. Under these conditions, the nanosheets form continuous CO_2 permeation pathways along the fairly long CO_2-philic GO/pGO surface with reoriented water channels surrounding the 2D structure. Further loading of both these fillers resulted in a drop in CO_2 permeance as the volume fraction of GO phase increases. Both GO9 and pGO9 resulted in increased CO_2 permeance at all loadings; this phenomenon may be due to the smallest average flake size and better dispersion in the polymer matrix. However, the smaller flake sizes inhibit the formation of continuous permeation pathways similar to GO6/pGO6 nanosheets. Hence CO_2 transport in these hybrids is reliant mainly on the polymer property changes as discussed earlier. Interestingly, at 0.2 wt% loading, all hybrids (both GO and pGO) had little influence over CO_2/N_2 selectivity. This can be attributed to the low volume fraction of nanosheets in the hybrids to effectively hinder permeation of N_2 with longer transport pathways circumventing the laminates. Under high loading of 0.5 wt%, all GO-based hybrids showcased a marginally increased CO_2/N_2 selectivity (from 32 to 38) owing to higher effective resistance to N_2 permeation when compared to CO_2 (Fig. 8A). The corresponding pGO hybrids had a similar effect on CO_2/N_2 selectivity, although to a lesser extent, due to the presence of non-selective pores.

3.5. Three-phase hybrid facilitated transport membranes for CO_2 separation

In an attempt to leverage the advantage of mobile carriers in HFTMs, 0.2 wt% of pGO was dispersed in a polymer matrix containing 10 wt% [Emim][OAc] and 20 wt% ProK. The compositions were chosen according to the optimal composition detected in the

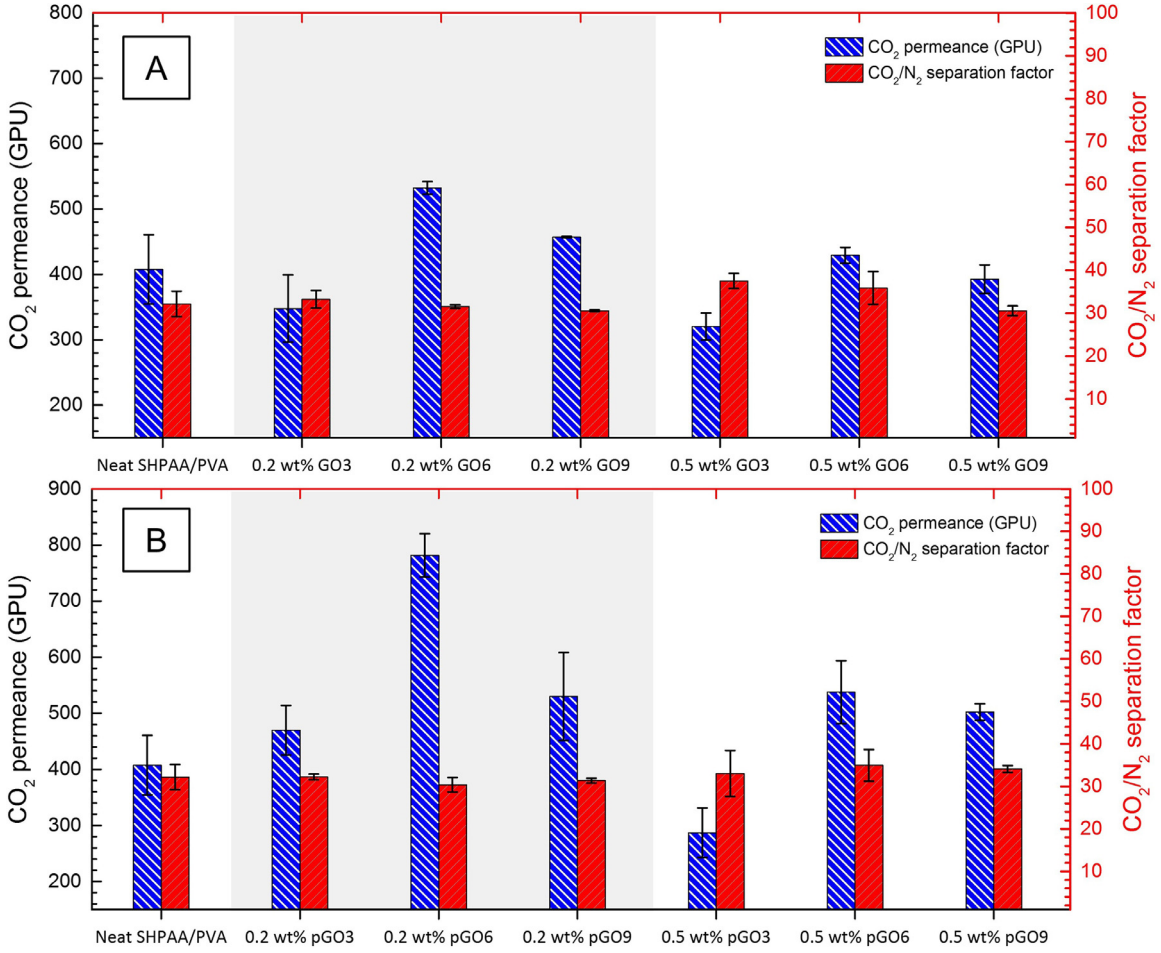

Fig. 8. CO_2/N_2 mixed gas permeation performance of various hybrid membranes containing (A) 0.2 wt% GO and 0.5 wt% GO (B) 0.2 wt% pGO and 0.5 wt% pGO measured at 35 °C.

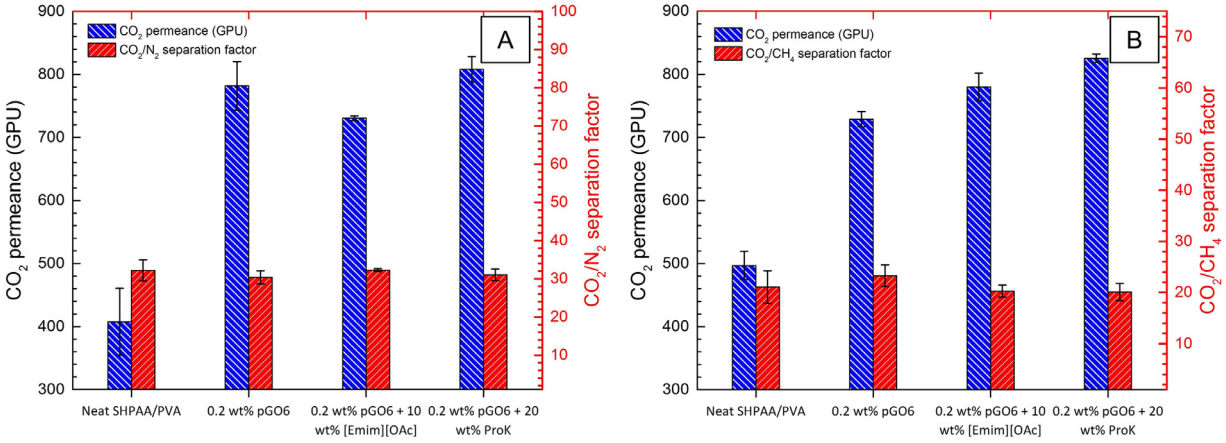

Fig. 9. Mixed gas permeation performance of various HFTMs measured at 35 °C for (A) CO_2/N_2 gas pair at 1.7 bar and (B) CO_2/CH_4 gas pair at 2 bar.

experiments and reported in the previous sections. The resulting three-phase HTFMs had a small increased performance for CO_2/N_2 separation only in the case of ProK containing membranes, increasing the CO_2 permeance up to 810 GPU as seen in Fig. 9A. This phenomenon can be a result of increased reactive species making use of distributed water channels made available by the pGO fillers in the polymer matrix. Such behaviour is better pronounced with CO_2/CH_4 separation performances, as seen in Fig. 9B. For these tests, the feed gas consisting of 40/60 v/v CO_2/CH_4 mixture was used, mimicking typical biogas composition [52,53]. Both mobile carriers containing membranes were characterized with a marked increase in CO_2 permeance while the CO_2/CH_4 separation factor remained constant around 20. The HFTM containing 0.2 wt% pGO6 with 20% ProK peaked at a CO_2 permeance of 825 GPU with a CO_2/CH_4 separation factor of 20, while the neat polymer had a CO_2 permeance of 497 GPU with a CO_2/CH_4 separation factor of 21 at a feed pressure of 2 bar. The corresponding HFTM containing 0.2 wt% pGO6 without mobile carriers was limited to 727 GPU

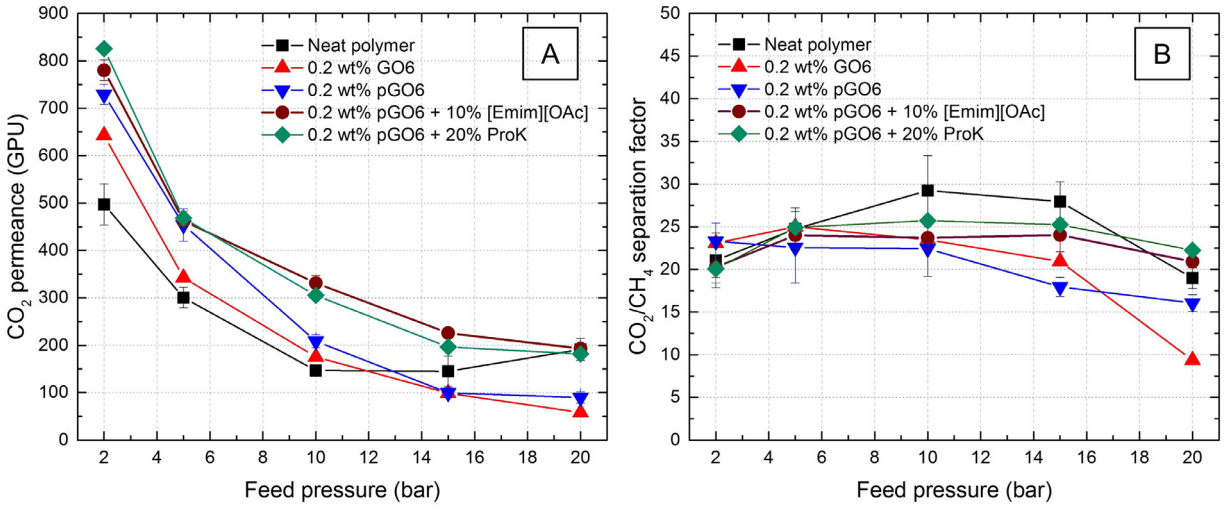

Fig. 10. CO_2/CH_4 mixed gas permeation performance of various 0.2 wt% HFTMs measured at 35 °C.

with CO_2/CH_4 feed gas mixture. A similar increase in CO_2 permeance of 10% [Emim][OAc] containing membrane up to 782 GPU was observed. The mobile carriers containing membranes exhibited an increased CO_2 permeance at the total upstream pressure of 2 bar with the CO_2/CH_4 feed mixtures due to the increased partial pressure CO_2 and lower stage cut (higher feed flow).

3.6. Influence of feed pressure in hybrid facilitated transport membranes

Investigating the effect of feed pressure on the permeation performance of a facilitated transport membrane is a common approach to examine the carrier saturation phenomenon, the characteristic feature commonly used to confirm the facilitated transport mechanism. It also allows to explore the membranes for applications at elevated pressures, like biogas upgrading, natural gas sweetening and pre-combustion CO_2 capture, which aids in optimizing process design of membrane-based separation units [52].

Herein, the effect of feed pressure on the CO_2/CH_4 separation performance of the fabricated three-phase HFTMs was studied by varying feed pressures. The upstream pressure was increased from 2 bar to a maximum of 20 bar. Increasing feed pressure led to further distinguishable separation performance based on the composition of HFTMs. Facilitated transport membranes are characterized with carrier saturation phenomenon at a high partial pressure of CO_2 in the feed. Since the availability of fixed CO_2 carriers (amine groups) in the polymer matrix is limited, increasing CO_2 partial pressure in the feed gas leads to carrier saturation, hence decreases the CO_2 permeance. Consequently, in all the systems discussed in this work, increasing pressure in the feed side reflects a drop in permeance of CO_2, as seen in Fig. 10, which is observed for typical facilitated transport membranes [25]. Interestingly, the membranes with loading 2D fillers, both GO6 and pGO6, exhibited increased resistance to carrier saturation phenomenon, especially at the pressures of 5 bar and 10 bar, which can be attributed to increased water retention due to reinforcement of matrix by the high aspect ratio nanosheets. Thus, the corresponding CO_2 permeances remained at 340 GPU and 450 GPU when compared with neat polymer at 300 GPU at 5 bar, which is typical operating pressure for biogas upgrading [54]. However, this resistance seemed to be less prominent at the higher pressures of 15 bar and 20 bar where neat polymer recorded higher permeances. This behaviour can be attributed to CO_2-induced swelling in the neat polymer, which is possibly delayed in all nanofiller-containing HFTMs due to distributed polymer chain packing. Regardless, the three-phase HFTMs that contained mobile carriers showcased further resistance to the carrier saturation phenomenon due to the increase of available CO_2 carriers, as expected. The effect remains evident across the entire pressure range of testing for both 10 wt% [Emim][OAc] and 20 wt% Pro-K loaded membranes. These membranes showcased a CO_2 permeance of 463 GPU and 468 GPU and CO_2/CH_4 separation factors of 24 and 25, respectively, at 5 bar.

4. Conclusions

Three-phase hybrid facilitated transport membranes containing GO-based 2D fillers and CO_2-philic mobile carriers in ultrathin selective layers were successfully fabricated and tested. GO-based fillers were found to benefit HFTMs to increase the CO_2 separation properties depending on their lateral dimensions and loading. pGO fillers derived from size-optimized GO nanosheets enhanced CO_2 permeation effectively at a loading of 0.2 wt%. These HFTMs were characterized with a high CO_2 permeance of 780 GPU and a corresponding CO_2/N_2 separation factor of 30. Facilitated transport membranes with mobile carriers that reversibly react with CO_2 were also fabricated as TFC hollow fibers. It was found that the mobile carriers ProK and [Emim][OAc] were able to improve the separation performance of the SHPAA/PVA membrane due to their high mobility and reversible interaction with CO_2 to form bicarbonate/carbonate species and carbene-CO_2 adducts, respectively. As a new concept, three-phase hybrid facilitated transport membranes were fabricated and the resulting membranes exhibited a CO_2 permeance of 825 GPU. These membranes were evaluated for both CO_2/N_2 and CO_2/CH_4 gas pairs and the separation factor was found to be 31 for CO_2/N_2 and 20 for CO_2/CH_4. Due to the relative increase in the content of CO_2-philic species and reinforcement with the addition of pGO, these three-phase HFTMs were stable for feed pressures of up to 20 bar and exhibited increased resistance to carrier saturation phenomena. This high stability and gas separation performance, when combined with easily scalable hollow fiber configuration, establishes the commercial viability of the fabricated membranes for CO_2 separation applications.

Declaration of Competing Interest

The authors declare that they have no known competing financial interests or personal relationships that could have appeared to influence the work reported in this paper.

CRediT authorship contribution statement

Saravanan Janakiram: Conceptualization, Methodology, Writing - original draft, Writing - review & editing. **Juan Luis Martín Espejo:** Validation, Investigation. **Karen Karolina Høisæter:** Resources, Investigation. **Arne Lindbråthen:** Resources, Writing - review & editing. **Luca Ansaloni:** Writing - review & editing. **Liyuan Deng:** Writing - review & editing, Project administration, Funding acquisition.

Acknowledgements

This work is a part of the NANOMEMC2 project supported by the European Union's Horizon 2020 Research and Innovation program under Grant Agreement n° 727734 and the FaT H2 project supported by the Norwegian Research Council (No. 294533). The authors thank Dr. Rany Miranti for discussions on the Raman Spectroscopy. Ricardo Wanderley and Prof. Hanna Knuutila are gratefully acknowledged for the discussions on mobile carriers. We thank Prof. Ho Bum Park and his group for the knowledge transfer in GO modification. The Research Council of Norway is acknowledged for the support to the Norwegian Micro- and Nano-Fabrication Facility, NorFab, project number 245963/F50.

Supplementary materials

Supplementary material associated with this article can be found, in the online version, at doi:10.1016/j.apmt.2020.100801.

References

[1] S. Janakiram, M. Ahmadi, Z. Dai, L. Ansaloni, L. Deng, Performance of nanocomposite membranes containing 0D to 2D nanofillers for CO_2 separation: a review, Membranes (Basel) (2018) 8, doi:10.3390/membranes8020024.
[2] W.M. McDanel, M.G. Cowan, N.O. Chisholm, D.L. Gin, R.D. Noble, Fixed-site–carrier facilitated transport of carbon dioxide through ionic-liquid-based epoxy-amine ion gel membranes, J. Memb. Sci. 492 (2015) 303–311.
[3] Y. Zhang, J. Sunarso, S. Liu, R. Wang, Current status and development of membranes for CO_2/CH_4 separation: a review, Int. J. Greenh. Gas Control. 12 (2013) 84–107, doi:10.1016/j.ijggc.2012.10.009.
[4] D.M. D'Alessandro, B. Smit, J.R. Long, Carbon dioxide capture: prospects for new materials, Angew. Chemie - Int. Ed. 49 (2010) 6058–6082, doi:10.1002/anie.201000431.
[5] L.M. Robeson, The upper bound revisited, J. Memb. Sci. 320 (2008) 390–400, doi:10.1016/j.memsci.2008.04.030.
[6] B.D. Freeman, Basis of permeability/selectivity tradeoff relations in polymeric gas separation membranes, Macromolecules 32 (1999) 375–380, doi:10.1021/ma9814548.
[7] H.B. Park, J. Kamcev, L.M. Robeson, M. Elimelech, B.D. Freeman, Maximizing the right stuff: the trade-off between membrane permeability and selectivity, Science (80) 356 (2017) eaab0530, doi:10.1126/science.aab0530.
[8] M. Ahmadi, S. Janakiram, Z. Dai, L. Ansaloni, L. Deng, Performance of mixed matrix membranes containing porous two-dimensional (2D) and three-dimensional (3D) fillers for CO_2 separation: a review, Membranes (Basel) 8 (2018) 50, doi:10.3390/membranes8030050.
[9] Y. Han, W.S.W. Ho, Recent advances in polymeric membranes for CO_2 capture, Chinese J. Chem. Eng. 26 (2018) 2238–2254, doi:10.1016/j.cjche.2018.07.010.
[10] J. Wu, S. Japip, T.S. Chung, Infiltrating molecular gatekeepers with coexisting molecular solubility and 3D-intrinsic porosity into a microporous polymer scaffold for gas separation, J. Mater. Chem. A. 8 (2020) 6196–6209, doi:10.1039/c9ta12028a.
[11] J. Wu, J. Liu, T.-S. Chung, Structural tuning of polymers of intrinsic microporosity via the copolymerization with macrocyclic 4- tert -butylcalix[4]arene for enhanced gas separation performance, Adv. Sustain. Syst. 2 (2018) 1800044, doi:10.1002/adsu.201800044.
[12] R.W. Baker, Future directions of membrane gas separation technology, Ind. Eng. Chem. Res. 41 (2002) 1393–1411, doi:10.1021/ie0108088.
[13] G. Dong, H. Li, V. Chen, Challenges and opportunities for mixed-matrix membranes for gas separation, J. Mater. Chem. A. 1 (2013) 4610–4630, doi:10.1039/C3TA00927K.
[14] Z. Dai, J. Deng, Q. Yu, R.M.L. Helberg, S. Janakiram, L. Ansaloni, L. Deng, Fabrication and evaluation of bio-based nanocomposite TFC hollow fiber membranes for enhanced CO_2 capture, ACS Appl. Mater. Interfaces. 11 (2019) 10874–10882, doi:10.1021/acsami.8b19651.
[15] C.Z. Liang, W.F. Yong, T.S. Chung, High-performance composite hollow fiber membrane for flue gas and air separations, J. Memb. Sci. 541 (2017) 367–377, doi:10.1016/j.memsci.2017.07.014.
[16] L. Ansaloni, L. Deng, Advances in polymer-inorganic hybrids as membrane materials, 2016. 10.1016/B978-0-08-100408-1.00007-8.
[17] Y. Dai, J.R. Johnson, O. Karvan, D.S. Sholl, W.J. Koros, Ultem ®/ZIF-8 mixed matrix hollow fiber membranes for CO_2/N_2 separations, J. Memb. Sci. 401–402 (2012) 76–82, doi:10.1016/j.memsci.2012.01.044.
[18] P.D. Sutrisna, J. Hou, H. Li, Y. Zhang, V. Chen, Improved operational stability of Pebax-based gas separation membranes with ZIF-8: a comparative study of flat sheet and composite hollow fibre membranes, J. Memb. Sci. 524 (2017) 266–279, doi:10.1016/j.memsci.2016.11.048.
[19] Y. Zhang, Q. Shen, J. Hou, P.D. Sutrisna, V. Chen, Shear-aligned graphene oxide laminate/Pebax ultrathin composite hollow fiber membranes using a facile dip-coating approach, J. Mater. Chem. A. 5 (2017) 7732–7737, doi:10.1039/c6ta10395b.
[20] S. Janakiram, X. Yu, L. Ansaloni, Z. Dai, L. Deng, Manipulation of fibril surfaces in nanocellulose-based facilitated transport membranes for enhanced CO_2 capture, ACS Appl. Mater. Interfaces. 11 (2019) 33302–33313, doi:10.1021/acsami.9b09920.
[21] S. Janakiram, L. Ansaloni, S.-A. Jin, X. Yu, Z. Dai, R.J. Spontak, L. Deng, Humidity-responsive molecular gate-opening mechanism for gas separation in ultraselective nanocellulose/il hybrid membranes, Green Chem. 22 (2020) 3546–3557, doi:10.1039/D0GC00544D.
[22] S. Janakiram, J. Luis Martín Espejo, X. Yu, L. Ansaloni, L. Deng, Facilitated transport membranes containing graphene oxide-based nanoplatelets for CO_2 separation: effect of 2D filler properties, J. Memb. Sci. (2020) 118626 In press, doi:10.1016/j.memsci.2020.118626.
[23] J. Shen, M. Zhang, G. Liu, K. Guan, W. Jin, Size effects of graphene oxide on mixed matrix membranes for CO_2 separation, AIChE J. 62 (2016) 2843–2852, doi:10.1002/aic.15260.
[24] L. Deng, M.B. Hagg, Carbon nanotube reinforced PVAm/PVA blend FSC nanocomposite membrane for CO_2/CH_4 separation, Int. J. Greenh. Gas Control. 26 (2014) 127–134, doi:10.1016/j.ijggc.2014.04.018.
[25] Y. Zhao, B.T. Jung, L. Ansaloni, W.S.W. Ho, Multiwalled carbon nanotube mixed matrix membranes containing amines for high pressure CO_2/H_2 separation, J. Memb. Sci. 459 (2014) 233–243, doi:10.1016/j.memsci.2014.02.022.
[26] Z. Dai, J. Deng, L. Ansaloni, S. Janakiram, L. Deng, Thin-film-composite hollow fiber membranes containing amino acid salts as mobile carriers for CO_2 separation, J. Memb. Sci. (2019), doi:10.1016/j.memsci.2019.02.023.
[27] H. Lee, S.C. Park, J.S. Roh, G.H. Moon, J.E. Shin, Y.S. Kang, H.B. Park, Metal-organic frameworks grown on porous planar template with exceptionally high surface area: promising nanofiller platforms for CO_2 separation, J. Mater. Chem. A. 5 (2017) 22500–22505, doi:10.1039/C7TA06049A.
[28] Y. Xu, Z. Lin, X. Zhong, X. Huang, N.O. Weiss, Y. Huang, X. Duan, Holey graphene frameworks for highly efficient capacitive energy storage, Nat. Commun. 5 (2014) 1–8, doi:10.1038/ncomms5554.
[29] J. Wang, Y. Wang, Y. Zhang, A. Uliana, J. Zhu, J. Liu, B. Van Der Bruggen, Zeolitic imidazolate framework/graphene oxide hybrid nanosheets functionalized thin film nanocomposite membrane for enhanced antimicrobial performance, ACS Appl. Mater. Interfaces 8 (2016) 25508–25519, doi:10.1021/acsami.6b06992.
[30] P.T. Lan Huong, N. Tu, H. Lan, L.H. Thang, N. Van Quy, P.A. Tuan, N.X. Dinh, V.N. Phan, A.T. Le, Functional manganese ferrite/graphene oxide nanocomposites: Effects of graphene oxide on the adsorption mechanisms of organic MB dye and inorganic As(v) ions from aqueous solution, RSC Adv. 8 (2018) 12376–12389, doi:10.1039/c8ra00270c.
[31] K. Erickson, R. Erni, Z. Lee, N. Alem, W. Gannett, A. Zettl, Determination of the local chemical structure of graphene oxide and reduced graphene oxide, Adv. Mater. 2 (2010) 4467–4472, doi:10.1002/adma.201000732.
[32] A. Liscio, K. Kouroupis-Agalou, X.D. Betriu, A. Kovtun, E. Treossi, N.M. Pugno, G. De Luca, L. Giorgini, V. Palermo, Evolution of the size and shape of 2D nanosheets during ultrasonic fragmentation, 2D Mater 4 (2017) 025017, doi:10.1088/2053-1583/aa57ff.
[33] Z.Y. Xia, S. Pezzini, E. Treossi, G. Giambastiani, F. Corticelli, V. Morandi, A. Zanelli, V. Bellani, V. Palermo, The exfoliation of graphene in liquids by electrochemical, chemical, and sonication-assisted techniques: a nanoscale study, Adv. Funct. Mater. 23 (2013) 4684–4693, doi:10.1002/adfm.201203686.
[34] U. Khan, A. O'Neill, M. Lotya, S. De, J.N. Coleman, High-concentration solvent exfoliation of graphene, Small 6 (2010) 864–871, doi:10.1002/smll.200902066.
[35] B.D. Ossonon, D. Bélanger, Synthesis and characterization of sulfophenyl-functionalized reduced graphene oxide sheets, RSC Adv. 7 (2017) 27224–27234, doi:10.1039/c6ra28311j.
[36] N. Sharma, V. Sharma, Y. Jain, M. Kumari, R. Gupta, S.K. Sharma, K. Sachdev, Synthesis and characterization of graphene Oxide (GO) and reduced graphene oxide (rGO) for gas sensing application, Macromol. Symp. 372 (2017) 1700006, doi:10.1002/masy.201700006.
[37] F. Tuinstra, J.L. Koenig, Raman spectrum of graphite, J. Chem. Phys. (1970) 53, doi:10.1063/1.1674108.
[38] L.M. Malard, M.A. Pimenta, G. Dresselhaus, M.S. Dresselhaus, Raman spectroscopy in graphene, Phys. Rep. 473 (2009) 51–87, doi:10.1016/j.physrep.2009.02.003.
[39] R.J. Nemanich, S.A. Solin, First- and second-order Raman scattering from finite-size crystals of graphite, Phys. Rev. B 20 (1979) 392, doi:10.1103/PhysRevB.20.392.
[40] C.H. Lui, L.M. Malard, S. Kim, G. Lantz, F.E. Laverge, R. Saito, T.F. Heinz, Observation of layer-breathing mode vibrations in few-layer graphene through combination raman scattering, Nano Lett. 12 (2012) 5539–5544, doi:10.1021/nl302450s.

[41] A.C. Ferrari, J. Robertson, Origin of the 1150−cm−1 Raman mode in nanocrystalline diamond, Phys. Rev. B - Condens. Matter Mater. Phys. 63 (2001) 1–4, doi:10.1103/PhysRevB.63.121405.
[42] X. Díez-Betriu, S. Álvarez-García, C. Botas, P. Álvarez, J. Sánchez-Marcos, C. Prieto, R. Menéndez, A. De Andrés, Raman spectroscopy for the study of reduction mechanisms and optimization of conductivity in graphene oxide thin films, J. Mater. Chem. C 1 (2013) 6905–6912, doi:10.1039/c3tc31124d.
[43] A.A.K. King, B.R. Davies, N. Noorbehesht, P. Newman, T.L. Church, A.T. Harris, J.M. Razal, A.I. Minett, A new raman metric for the characterisation of graphene oxide and its derivatives, Sci. Rep. 6 (2016), doi:10.1038/srep19491.
[44] L. Deng, T.J. Kim, M.B. Hägg, Facilitated transport of CO_2 in novel PVAm/PVA blend membrane, J. Memb. Sci. 340 (2009) 154–163, doi:10.1016/j.memsci.2009.05.019.
[45] Y. Zhao, W.S.W. Ho, CO_2-selective membranes containing sterically hindered amines for CO_2/H_2 separation, Ind. Eng. Chem. Res. 52 (2013) 8774–8782, doi:10.1021/ie301397m.
[46] G. Gurau, H. Rodríguez, S.P. Kelley, P. Janiczek, R.S. Kalb, R.D. Rogers, Demonstration of chemisorption of carbon dioxide in 1,3-dialkylimidazolium acetate ionic liquids, Angew. Chemie - Int. Ed. 50 (2011) 12024–12026, doi:10.1002/anie.201105198.
[47] C.A. Hall, K.A. Le, C. Rudaz, A. Radhi, C.S. Lovell, R.A. Damion, T. Budtova, M.E. Ries, Macroscopic and microscopic study of 1-Ethyl-3-methylimidazolium acetate-water mixtures, J. Phys. Chem. B. 116 (2012) 12810–12818, doi:10.1021/jp306829c.
[48] H. Rodríguez, G. Gurau, J.D. Holbrey, R.D. Rogers, Reaction of elemental chalcogens with imidazolium acetates to yield imidazole-2-chalcogenones: direct evidence for ionic liquids as proto-carbenes, Chem. Commun. 47 (2011) 3222–3224, doi:10.1039/c0cc05223j.
[49] J.A. Lim, D.H. Kim, Y. Yoon, S.K. Jeong, K.T. Park, S.C. Nam, Absorption of CO_2 into aqueous potassium salt solutions of l -alanine and l -proline, Energy Fuels 26 (2012) 3910–3918, doi:10.1021/ef300453e.
[50] Y.T. Chang, R.B. Leron, M.H. Li, Carbon dioxide solubility in aqueous potassium salt solutions of L-proline and DL-α-aminobutyric acid at high pressures, J. Chem. Thermodyn. 83 (2015) 110–116, doi:10.1016/j.jct.2014.12.010.
[51] A.T. Dideikin, A.Y. Vul', Graphene oxide and derivatives: the place in graphene family, Front. Phys. 6 (2019) 149, doi:10.3389/fphy.2018.00149.
[52] L. Deng, M.B. Hägg, Techno-economic evaluation of biogas upgrading process using CO_2 facilitated transport membrane, Int. J. Greenh. Gas Control. 4 (2010) 638–646, doi:10.1016/j.ijggc.2009.12.013.
[53] Q. Sun, H. Li, J. Yan, L. Liu, Z. Yu, X. Yu, Selection of appropriate biogas upgrading technology-a review of biogas cleaning, upgrading and utilisation, Renew. Sustain. Energy Rev. 51 (2015) 521–532, doi:10.1016/j.rser.2015.06.029.
[54] N. Abatzoglou, S. Boivin, A review of biogas purification processes, Biofuels Bioprod. Biorefining. 3 (2009) 42–71, doi:10.1002/bbb.117.